Title: Structural, morphological and photometric properties of sonochemically synthesized Eu^{3+} doped Y_2O_3 nanophosphor for optoelectronic devices

Authors: K.N. Venkatachalaiah, H. Nagabhushana, G.P. Darshan, R.B. Basavaraj, B.Daruka Prasad, S.C. Sharma

PII: S0025-5408(16)32544-2
DOI: http://dx.doi.org/doi:10.1016/j.materresbull.2017.06.025
Reference: MRB 9408

To appear in: *MRB*

Received date: 19-12-2016
Revised date: 11-6-2017
Accepted date: 16-6-2017

Please cite this article as: K.N.Venkatachalaiah, H.Nagabhushana, G.P.Darshan, R.B.Basavaraj, B.Daruka Prasad, S.C.Sharma, Structural, morphological and photometric properties of sonochemically synthesized Eu3+ doped Y2O3 nanophosphor for optoelectronic devices, Materials Research Bulletinhttp://dx.doi.org/10.1016/j.materresbull.2017.06.025

Structural, morphological and photometric properties of sonochemically synthesized Eu^{3+} doped Y_2O_3 nanophosphor for optoelectronic devices

K. N. Venkatachalaiah[1, 2], H. Nagabhushana[3,*], G.P. Darshan[4], R.B. Basavaraj[3], B. Daruka Prasad[5], S.C. Sharma[6, 7]

[1]Department of Physics, Amrita School of Engineering, Amrita Vishwavidyapeetham, Amrita university, Bengaluru- 560035, India
[2]Research and Development Center, Bharathiar University, Coimbatore 641046, India
[3]Prof. C.N.R. Rao Centre for Advanced Material Science, Tumakuru University, Tumakuru-572103, India
[4]Department of Physics, Acharya Institute of Graduate Studies, Bangalore 560 107, India
[5] Department of Physics, B.M.S. Institute of Technology and Management, VTU-Belagavi affiliated, Bengaluru-560 064, India
[6]Department of Mechanical Engineering, Jain University, Advisor, Jain group of Institutions, Bengaluru- 560069, India
[7]Advisor, Avinashilingam University for Women, Coimbatore-641043, Tamilnadu, India

Graphical abstarct

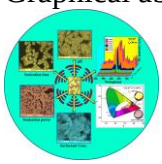

Research highlights

- Y_2O_3:Eu^{3+} nanophosphors were prepared by modified sonochemical route using *A.V.* gel.
- Reported the effects of pH, time and concentration of bio-surfactant on the morphologies.
- Synthesis route is rapid, bio-compatible, cost-effective useful for industrial application.
- Photometric properties reveals the use of phosphor for optoelectronics applications.

Abstract

Synthesis of Eu^{3+}doped Y_2O_3 nanophosphors via modified sonochemical method was presented. Morphologies of the prepared products were analyzed with respect to the

influential parameters during the preparation time. The photoluminescence (PL) emission spectra exhibits several peaks at ~ 537 nm, 598 nm, 613 nm and 662 nm attributed to $^5D_0 \rightarrow {}^7F_J$ (J = 0, 1, 2 & 3) transitions of Eu^{3+} ions in the host lattice. The types of energy transfer between the Eu^{3+} ions were responsible for concentration quenching confirms the electric *dipole–quadrupole* interaction among the ions. The Judd-Ofelt intensity parameters and other radiative properties were estimated by using PL emission spectra. The photometric characteristics of the prepared samples indicate that the color co-ordinates were tune towards pure red emission with color purity ~ 88 %. The results signified that the prepared Y_2O_3:Eu^{3+} nanophosphor was a potential amber phosphor for solid state and LED's applications.

Key words: Sonochemistry; Photoluminescence; Judd-Ofelt analysis; LED displays.

* Corresponding author: +91- 9945954010, E-mail: bhushanvlc@gmail.com
(H. Nagabhushana)

1. Introduction

Lanthanide ions doped oxides were referred to be very promising fluorescent materials because of their extraordinary physico-chemical properties. By configuring the 4f electronic shells of the lanthanides, the physical and chemical properties of these materials can be tuned easily. Y_2O_3 was considered as a proficient host for rare earth (RE) ions due to similar chemical properties and near ionic radii of Y^{3+} ions with RE ions. These were showed potential applications viz., solar cells, display devices and opt-electronic devices due to their properties such as narrow emission lines and long luminescent lifetime [1-3]. Europium (Eu^{3+}) ions when doped into the Y_2O_3 host; it shows drastic increase in its luminous efficiency due to the tunable energy transfer between the Eu^{3+} ions and the host matrix and also enhances the stability as well as the emission efficiency of the phosphor [4-6].

There are various methods available for the synthesis of nanophosphors with increased brightness and higher decay time [7, 8]. But there is a need of finding the preparation methods which are environmental friendly is one of the challenges for material scientists. Recently 'green' approaches by using ionic liquids and bio-templates were showed to be alternative efficient approaches in controlling the size, shape and surface structure of nanophosphors [9, 10].

Bartholomew et al [11] identified the physical mechanisms responsible for the optical homogeneous broadening in Eu^{3+}:Y_2O_3 nanoparticles. These results allow the integrated rare-earth ion quantum optics to be pursued at a submicron scale. It opens up path for greater scaling of quantum technology. Anh et al [12] showed a solution for an increase in color rendering index of multi-chip white LED packages using Y_2O_3:Eu^{3+} phosphor material. They used LightTools program and the Monte Carlo method to arrive at the conclusions. The highest lumen output is achieved at low Y_2O_3:Eu^{3+} concentration and this material showed for manufacturing of efficient white LED packages. Jin et al [13] synthesized Y_2O_3 phosphor material by conventional solid state method along with Eu^{3+} and Bi^{3+} as dopants. They obtained the CIR coordinates and CCT values which are very close to the white light, hence they promised that the prepared samples are good materials for ultraviolet excitation white LED application. Wang et al [14] analyzed pressure induced microstructural variations in Y_2O_3/Eu^{3+} and Y_2O_3/Eu^{3+}/Mg^{2+} nanorods by Raman and photoluminescence spectra. They showed the transformation to amorphous phase at 24 GPa. Mg^{2+} ions play a critical role in reducing the decrease in crystal iconicity under high pressure. Bakovets et al [15] developed the algorithm for estimating E_g values of samples annealed at 700 and 1300 °C and observed the changes in E_g. They concluded that while PL of the materials, we must exclude the emission spectrum in fundamental absorption edge (FAE) region. The proposed technique can be used to process diffused reflectance (DR) spectra that do not cut off the luminescence

signal at the spectrophotometer output. Li et al [16] investigated the lattice behaviour of cubic Y_2O_3/Eu^{3+} nanotubes under high pressure of up to 20 GPa. The local disorder of the lattice was due to the pressure induced deformation of the YO_6 octahedra under the high pressure. Among the various synthesis routes, ultrasound assisted sonochemical route was showed better path to obtain high purity, high yield, size tunable and convenient reaction rate. In this method, nucleation of acoustic resonating bubbles followed by impulsive collapse of these bubbles and breaking of the regular chemical bonds leads to obtain superstructured materials [17 – 21]. During acoustic resonance, the diffusion of the reactant molecules was controlled by the liquid and resonating ultrasonic waves.

The present work addresses the synthesis of $Y_2O_3:Eu^{3+}$ (1-11 mol %) nanophosphor via ultrasound assisted sonochemical route using extract of Aloe Vera (*A.V.*) gel as a bio-surfactant. Structural and photometric properties of the prepared compounds were also reported.

2. Experimental

2.1 Materials and methods

The precursors used in the present study were yttrium nitrate ($Y(NO_3)_3:H_2O$), europium nitrate ($Eu(NO_3)_3.5H_2O$) and NaOH procured from Sigma Aldrich. *A.V.* gel was extracted from *A.V.* plants grown in and around the Tumkur University Campus (13.33778° N, 77.12028° E) in the month of June 2016. 20 ml of thick gel of *A.V.* was diluted by adding 80 ml of double distilled water and kept on a magnetic stirrer to get homogeneous mixture of 5% W/V of surfactant. For the preparation of $Y_2O_3:Eu^{3+}$ (1 mol %), 3.83 g of yttrium nitrate and 0.0428 g of europium nitrate were dissolved in 50 ml of double distilled water and mixed homogeneously using magnetic stirrer. Further, different concentration of *A.V.* gel (5 % to 30 % W/V) was added to the resultant mixture slowly and pH levels (1, 5, 7, and 9) of the

solutions were maintained by adding drop wise NaOH (1M) solution under constant stirring using magnetic stirrer. After obtaining the clear solution along with desired pH, the solution mixture was stirred ultrasonically (ultrasonic frequency ~ 20 kHz, power ~ 300 W) at fixed temperature of 80 °C and by varying sonication time (1 - 6 h). Later, the solution was kept undisturbed until a white precipitate was formed. Finally, precipitate was filtered and washed several times by distilled water and ethanol to remove any unreacted materials. Similarly, the same procedure was followed for remaining concentrations of Eu^{3+} (3 - 11 mol %) and for different experimental parameters. The precipitated powder was dried at 80 °C for 2 h in an oven and further calcined at ~ 700 ºC for 3h. The schematic diagram of Eu^{3+} doped Y_2O_3 nanophosphor synthesized by ultrasound assisted sonochemical method was shown in Fig.1.

2.2. Characterization

A shimadzu (XRD-7000) powder diffractometer was used to obtain PXRD profiles of the prepared product in the 2θ range (20-70°) with scan rate of 0.02 $°s^{-1}$ using Cu-Kα (λ = 1.5418 Å) radiation. The morphological studies were carried out by Hitachi (TM - 3000 and H-8100). The powder samples were supported on aluminium stubs and then coated with gold by plasma prior to measurement. The PL excitation and emission spectra of the prepared samples were recorded by using Fluorolog-3 Jobin Yvon Spectroflourimeter with 450 W Xenon lamp as an excitation source in the range 500 – 750 nm at RT.

3. Result and discussions

Fig.2 (a) shows the PXRD patterns of Y_2O_3:Eu^{3+} (1-11 mol %) nanophosphor. The peaks located at (222), (400), (134), (440) and (622) corresponds to the body - centered cubic phase of Y_2O_3 lattice with space group Ia-3 and were in good agreement with the standard JCPDS card no. 83-0134 [22]. The highest intense peak at ~ 29.5° corresponding to the plane (222) was shifts towards lower angle side with increase of Eu^{3+} dopant concentration was shown in

Fig.2 (a). The peak shifting was due to increase of the inter-planar distance (d) after doping and can be explained by mismatch of ionic radii and strain developed in the lattice. Dopant ions occupied lattice sites of Y^{3+} and lead to increase of inter-atomic distance and expansion in lattice constants. Further, the average crystallite sizes were estimated for (222), (400), (134), (440) and (622) peaks using Debye Scherrer's relation and listed in Table 1. The broadening of PXRD peaks was mainly related to strain present in the samples. Williamson–Hall (W-H) fitting equation (Fig. 2(b)) was used to estimate the crystallite size and microstrain estimated as reported elsewhere [23, 24] and tabulated in Table 1.

The cubic structure contains two symmetry cations sites C_2 and C_{3i}, both co-ordinates with six–fold with oxygen, as shown in Fig.2 (c). C_2 and C_{3i} sites were arranged over two Wyckoff positions 8b and 24d local symmetry respectively. Wyckoff 48e positions were occupied by oxygen ions. In an optical approach, C_{3i} site has a centre of inversion symmetry and it allows only magnetic dipole transitions while C_2 site does not have inversion symmetry and hence it allows both magnetic and electric dipole transitions. The cubic structure of the prepared samples was provided the statistical validity confirmed through structural refinement by using *Fullprof suite 3.0 Program*. In the refinement process, initially the positions of the peaks were corrected by refinements of zero-shift error. The least-square procedures were adopted for minimization of difference by using reliability index parameters weighted residual error (R_{wp}) and Bragg factor (R_B). Background was fitted with Chebyshev function (χ^2) of variable number of coefficients depending on its complexity. The refinement parameters like lattice constant, phase fractions, density, refined coefficients and goodness of fitment were tabulated in Table 2. Fig.2 (c) indicates that the results were good agreement with observed and calculated PXRD patterns. Goodness of fitment was found to be nearly equal to 1 in all cases. Further, for 5 mol % of Eu^{3+} ions, the X-ray density and Eu^{3+} occupancy at 8b-Wyckoff state are least whereas the oxygen occupancy at 48e-Wyckoff state

is highest when compared to the other mole % of Eu^{3+} ions. Fig 2(d) shows the good agreement of experimental and estimated values and inset of Fig. 2(C) shows the packing diagram of Y_2O_3:Eu^{3+} nanophosphor using diamond software [25]. The prepared Y_2O_3 nanophosphor has a cubic phase with a space group Ia-3 and point group symmetry m-3. The unit cell 16 units and 32 cations. To understand effective substitution of dopant Eu^{3+} ions at Y^{3+} symmetry site, the acceptable percentage difference was estimated by using relation reported elsewhere [26]. The ionic radii of Eu^{3+} and Y^{3+} ions were close to each other and estimated value of D_r was found to be ~ 5.2 %. This shows that dopant Eu^{3+} ions were substituted easily at Y^{3+} symmetry site.

Fig. 3 shows the effect of different sonication time on the morphology of the obtained Y_2O_3:Eu^{3+} (5 mol %) nanophosphor using 30 % W/V of biosurfactant *A.V.* gel and maintaining pH value of ~ 9. When 1 h sonication time, agglomerated microstructures were observed (Fig.3 (a)). With increase in sonication time to 2-3 h (Fig.3 (b & c)), size of agglomerated of microstructures was slightly reduced and begins to spherical microstructures. When sonication time was maintained to 4 - 6 h, better uniform spherical shaped microstructures were observed in Fig.3 (d, e & f). With further prolong of sonication time to 7 and 8 h, uniform spherical shaped structures were thriving themselves to form again agglomerated microstructures Fig.3 (g & h). From above results, reveal that optimal sonication time for the synthesis of fine spherical shaped microstructures was 6 h.

Fig.4 shows the SEM images of Y_2O_3:Eu^{3+} (5 mol %) nanophosphor synthesized with different concentration of *A.V.* gel (5% W/V, 10% W/V, 15% W/V, 20% W/V, 25% W/V and 30% W/V) while sonication time and pH were fixed at 6 h and 9 respectively. When the concentration of *A.V.* gel was 5 % - 15 % W/V, non-uniform particles were observed (Fig.4 (a, b& c). However, when the concentration of *A.V.* gel was increased to 20 % - 25 % W/V, small dumbbell shaped particles were obtained (Fig.4 (d & e). Further, increases of *A.V.* gel

concentration to ~ 30 % W/V, spherical shaped particles were observed in Fig.4 (f). These results evident that, the concentration of *A. V.* gel play an important role in tuning the morphology of the product.

Influence of pH on the morphological features of $Y_2O_3:Eu^{3+}$ (5 mol %) nanophosphor was depicted in Fig.5. It was witnessed that pH may greatly influence the morphology of the product. The triangular open faced cones like structures were observed when the pH was fixed to 1, while sonication time and concentration of *A.V.* gel were fixed at 6 h and 30 % W/V respectively. Again when the pH value was raised to 5, open faces of the cone were closed which is may be due to decrease in the hydrogen ion concentration which binds the particles together. When the pH value of the precursor solution was further increased to 7 and 9, the facets of the cones were almost closed leads to almost spherical shaped particles and smooth surface morphology was dominated (Fig. 5 (c & d). The effect of sonication power on morphology of the product when 6 h sonication time, 30 % W/V *A.V.* gel concentration and pH = 9 was also studied depicted as shown in Fig.6. Initially at lower sonication power (20 kHz), prepared compounds showed spherically shaped morphology along with small network of agglomeration (Fig.6 (a)) which is similar to the SEM images of Fig. 3(f), 4(f) and 5(d) cases. In all these cases, the experimental parameters were same leads to almost similar morphology but only the scale bars were different. The scale bar is varied because at the time of zooming the samples to various magnifications, marginal variations in the morphology exist always. When the sonication power was increased to 24 kHz, uneven shaped structures get separated and forms leaflet morphology (Fig.6 (b)). However, sonication power was increased to 26 kHz, leaflets undergoes self-assembly to form flower like morphology (Fig.6 (c)). Further, increase of sonication power to 28 kHz clear flower - like structures were observed (Fig. 6 (d)).

Fig.7 shows the pictorial representation for the formation of Y_2O_3: Eu^{3+} structures in presence of *A.V.* gel during ultrasound assisted sonochemical route. The *A.V.* gel contains many organic molecules including major constituents' viz. tetracontane (29.8 %), Guanosine (19 %), 1-phenyl etanone (13 %) and pentadecanoic acid (6.8 %) which primarily acts as surfactant molecules [27]. Even though surfactant molecules were having low melting and boiling points, molecules get decomposed / evaporated during heating at very high temperature but assisted usual crystallization before get separated from the inorganic masses. *A.V.* gel contents formed as efficient micelle, in which hydrophilic end of the molecules arranged as exterior and non-polar hydrophobic part become interior. The hydrophilic part of the micelle attached to the thus formed polar $Y(OH)_3$ under ultrasound leads to nucleation, crystallization and self –assembly to form different Y_2O_3:Eu^{3+} structures [28].

Fig.8 shows the SEM micrographs of Y_2O_3:Eu^{3+} (5 mol %) nanophosphor synthesized with different sonication time (2, 3, 5 and 6 h) without surfactant and pH of 9. It was clearly evident that, no definite shaped structures were observed for various sonication times. Aforementioned results evident that, ultrasound irradiation time, concentration of *A.V.* gel, sonication power and pH value were greatly influenced on morphology of the prepared Y_2O_3:Eu^{3+} (5 mol %) nanophosphor.

Fig.9 (a, b) shows the TEM images of Y_2O_3:Eu^{3+} (5 mol %) nanophosphor prepared with pH of 9 and sonication power of 20 kHz. The spherical shaped morphology of the prepared samples was observed. HRTEM image shown in Fig.9 (c) supports for the existence of twinned with stacking faults and other defects visible in the nano range which supports for the PXRD results also. From the image, it was evident that the obtained product was highly crystalline in nature and interplanar spacing (d) was found to be ~ 0.28 nm. The Fig.9 (d) shows the selected area electron diffraction (SAED) pattern of the Eu^{3+} (5 mol %) doped Y_2O_3 nanophosphor. The diffraction rings in SAED pattern specify the crystallinity of

the prepared product and were well indexed with (211), (222), (400), (411), (332), (440) and (622) planes which were due to cubic phase of the $Y_2O_3:Eu^{3+}$ (5 mol %) nanophosphor.

The excitation spectrum of $Y_2O_3:Eu^{3+}$ (5 mol %) nanophosphor was recorded in the range 300 - 500 nm at an emission wavelength 612 nm was shown in Fig.10 (a). The spectra shows sharp and intense peaks at ~ 364, 383, 397, 415, and 466 nm were attributed to $^7F_0 \rightarrow {}^5D_4$, $^7F_0 \rightarrow {}^5L_7$, $^7F_0 \rightarrow {}^5L_6$, $^7F_0 \rightarrow {}^5D_3$, and $^7F_0 \rightarrow {}^5D_2$ transitions of Eu^{3+} ions in the host lattice site respectively [29, 30]. Fig. 10 (b) shows the emission spectra of $Y_2O_3:Eu^{3+}$ (1-11 mol %) nanophosphor under 397 nm excitation wavelength at room temperature (RT). The spectra exhibit peaks at ~ 537, 598, 612 and 662 nm were attributed to $^5D_0 \rightarrow {}^7F_0$, $^5D_0 \rightarrow {}^7F_1$, $^5D_0 \rightarrow {}^7F_2$ and $^5D_0 \rightarrow {}^7F_3$ $4f^6$ configuration of Eu^{3+} ions, respectively [31, 32]. The spectral line split of 612 nm peak was observed and was due to local distortion induced by dopant ion concentration (Fig. 10 (b)).The energy level diagram of Eu^{3+} ions in Y_2O_3 host was shown in Fig.12 (a). The peak at 612 nm was electric –dipole transition $^5D_0 \rightarrow {}^7F_2$ which was much intense and hypersensitive in the host matrix. The weak emission peak at 598 nm was attributed to $^5D_0 \rightarrow {}^7F_1$ transition and ascribed to magnetic dipole transition which was insensitive to site symmetry. Asymmetry ratio (A_{21}) was used to determine the degree of distortion from the inversion symmetry of the local environment of the Eu^{3+} ions in the host was given by following equation [33]:

$$A_{21} = \frac{\int_{600}^{620} I_2 d\lambda}{\int_{575}^{596} I_1 d\lambda} \qquad \text{---------- (1)}$$

where I_1 and I_2; integrated intensity at ~ 612 and ~ 598 nm respectively. In the present case, the value of A_{21} for $Y_2O_3:Eu^{3+}$ (1-11 mol %) nanophosphor decreases with increase of Eu^{3+} concentration. The variation of A_{21} values with doping concentration can influence the luminescent property of a sample. It was evident that, intensity of emission peak (612 nm) was increased with increase of Eu^{3+} concentration up to 5 mol % and later diminishes. The

variation of PL intensity with Eu^{3+} ion concentration at 612 nm peak was shown in Fig. 11 (a).The diminishes in PL emission intensity was due to well-known self-concentration quenching phenomena which attributed to energy transfer among dopant Eu^{3+} ions in Y_2O_3 matrix. The distance between the two Eu^{3+} ions in Y_2O_3 host was estimated by using critical energy transfer distance relation [34]:

$$R_c = 2\left(3V/4\pi NX_c\right)^{1/3} \quad \text{---------- (2)}$$

where V; unit cell volume, X_c; critical concentration of Eu^{3+} ions and N; number of crystallographic sites per unit cell. In the present case, calculated value of R_c was found to be ~ 14.21 Å. The value of R_c was greater than 5 Å shows that electric multipolar interaction is the main reason of concentration quenching. The electric multipolar interaction involves dipole – dipole, dipole – quadrupole and quadrupole – quadrupole interactions. According to Dexter theory, the type electric multipolar interaction was estimated by using the following relation [35]:

$$\frac{I}{\chi} = K\left[1+\beta(\chi)^{\frac{Q}{3}}\right]^{-1} \quad \text{---------- (3)}$$

where χ ; concentration of Eu^{3+} ions, Q ; a constant of electric multipolar interaction and K & β ; constants for the given host crystal under the same excitation condition [36]. The value of *Q* was estimated by plotting log (I/χ) v/s log (χ) and was shown in Fig.12 (b). The figure clearly confirms that the relation was approximately linear and the value of slope was about -0.980. The calculated value Q was found to be 7.66 by linear fitting using Eq. (3) and was nearly equal to 8.This finding indicates that the charge transfer mechanism was due to dipole–quadrupole interaction for the concentration quenching in Y_2O_3:Eu^{3+} (1-11 mol %) nanophosphor.

Generally, different experimental parameters were more influenced on optical properties. Fig.10 (c) shows the PL emission spectra of Y_2O_3:Eu^{3+} (5 mol %) nanophosphor

synthesized at various pH values (1, 5, 7 and 9) under excitation wavelength of 397 nm. It can be observed from the figure that, PL intensity increases as pH value of the solution increases. Therefore, in the present case the maximum PL emission intensity was observed for pH value 9. Similarly, many experiments were carried out to explore the relationship between morphology and PL properties of the prepared samples. The PL emission spectra of Y_2O_3:Eu^{3+} (5 mol %) nanophosphor synthesized with various concentrations of *A.V.* gel (5%, 10%, 15%, 20%, 25% and 30% W/V) under λ_{Exci} = 397 nm at RT was depicted in Fig. 10 (d). The various morphologies of the samples will affect the scattering and absorption of incident light which leads to changes in the emission intensities. In Fig. 10 (b) and (c), the small split in the major peaks of the spectra were observed when the concentration of Eu^{3+} ions is less than 5 mol % . But when it is equal to or more than 5 mol % which altered the crystal field around Eu^{3+} ions led to the split in the major peak. Similar kinds of reports were reported in the literature also. As shown in Fig. 10 (d), the PL intensity increases with increase of concentration of *A.V.* gel and was due to fact that spherical shaped samples exhibits much higher PL intensity than dumbell shaped particles. The spherical shaped particles have higher surface area while in dumbell particles suffer from surface defect due lower affinity of luminescence ions on the surface resulting in diminish non – radioactive decay. Conversely, various changes in the morphology of the samples could alter the electronic structure, which influences the carriers to excite from valence band to conduction band and photon emission from the surface of the samples. Above results evidence that, tuning of morphology through different experimental parameters creates new avenue and emphasizes the importance of morphology control. The variation of PL intensity with various pH values and *A.V.* gel concentration at 612 nm peak was shown in Fig. 11 (b & c) respectively.

The Judd–Ofelt (J - O) analysis from PL emission spectra was a powerful tool for evaluating the radiative transition of RE ions in various hosts [37, 38]. J - O intensity

parameters (Ω_2 and Ω_4) explore the bonding character of RE ions with its surrounding ligands and site symmetry of dopant RE ions. The integrated radiative emission rates between two transitions $^5D_0$ and ^7F_J (J = 2, 4) was given by following relation [39].

$$\frac{A_{0\text{-}2,4}}{A_{0\text{-}1}} = \left[\frac{I_{0\text{-}2,4}}{I_{0\text{-}1}}\right]\left[\frac{h\nu_{0\text{-}1}}{h\nu_{0-2,4}}\right] \qquad \text{--------- (4)}$$

where $I_{0-2,4}$; the integrated emission intensity and $h\nu_{0\text{-}J}$; the energy corresponding to transition $^5D_0 \rightarrow {}^7F_J$ (J = 1, 2, 4). But due to small emission intensity of $^5D_0 \rightarrow {}^7F_0$ and $^5D_0 \rightarrow {}^7F_3$ transitions were neglected. Further, the magnetic-dipole radiative emission rate $A_{0\text{-}1}$ value was found to be ~ 50 s^{-1} [40]. The forced electric dipole transition as a function of J-O intensity parameters was expressed as:

$$A_{0\text{-}2,4} = \frac{64\pi^4\left(\nu_{0\text{-}2,4}\right)^3 e^2}{3hc^3}\left(\frac{1}{4\pi\varepsilon_0}\right)\chi \sum_{J=2,4}\Omega_J \left\langle {}^5D_0 \left| U^{(J)} \right| {}^7F_J \right\rangle^2 \qquad \text{----- (5)}$$

where $\chi = n(n^2+2)^2/9$; the Lorentz local field correction factor and n ; the refractive index of host lattice. The square matrix elements $\left\langle {}^5D_0 \left| U^{(J)} \right| {}^7F_2 \right\rangle^2 = 0.0032$ $\left\langle {}^5D_0 \left| U^{(J)} \right| {}^7F_4 \right\rangle^2 = 0.0023$ values were independent of chemical environment of the dopant Eu^{3+}ions [41]. Thus, by equating Eq. (4) and Eq. (5), intensity parameters (Ω_2 and Ω_4) of Y_2O_3:Eu^{3+} (1- 11 mol %) nanophosphor were evaluated and given in Table.3. The J-O intensity parameters Ω_2 and Ω_4 were due to short range and long-range effect respectively.

Further, by utilizing the J-O intensity parameters radiative parameters such as transition probabilities, radiative life time, branching ratio and stimulated emission cross-section were estimated according to literature [42, 43]. The radiative life-times (τ_{rad}) for an excited state (J) was calculated by using

$$\tau_{rad} = \frac{1}{\sum A\left(J - J'\right)} \qquad \text{------ (6)}$$

where the sum is taken over all final lower-lying states J'. These parameters were estimated and given in Tables.3 and 4. The stimulated emission cross-section is an important factor to predict the laser performance of a material and also the rate of the energy extraction from the lasing material. The calculated higher value of stimulated emission cross section of $^5D_0 \rightarrow {}^7F_2$ transition shows prepared samples exhibits low threshold and high gain laser applications and which can be used for good lasing action. The product of emission cross-section and effective bandwidth (σ_e x Δ_{eff})of the emission was highly useful in determining the bandwidth of the optical amplifier [44, 45]. The higher value of (σ_e x Δ_{eff}) was found to be ~ 7.15 corresponding to $^5D_0 \rightarrow {}^7F_4$ shows better amplifiers performance of the prepared samples. In addition, product (σ_e x τ_{rad}) plays a major role for better optical amplifier gain. The calculated optical gain of the Y_2O_3:Eu^{3+} (1- 11 mol %) nanophosphor provide good lasing action, high gain bandwidth and optical gain for amplifiers. Aforementioned results evident that the prepared Y_2O_3:Eu^{3+} (1- 11 mol %) nanophosphor can be highly useful for red emission laser applications and color display devices.

The color perception of human eye was expressed by mathematically in terms of CIE coordinates given by the Commission Internationale de L'Eclairage for illumination. In general, the emission color of any phosphor can be represented by the (*x, y*) chromaticity coordinates [46]. The CIE co-ordinates of Y_2O_3:Eu^{3+} (1- 11 mol %) nanophosphor were estimated using PL emission spectra and the values were listed in Table.5. The CIE chromaticity diagram of prepared samples was shown in Fig.12 (c). It was observed from figure that, the CIE co-ordinates ofY_2O_3: Eu^{3+} (1-11 mol %) nanophosphor were located in the orange red region and tuning towards National Television System Committee (NTSC) standard values of pure red color (0.67, 0.33) region.

The correlated color temperature (CCT) was one of the important parameter to know the color appearance of the light emitted by a source, relating its color with respect to a

reference light source when heated up to a specific temperature in Kelvin (K) [46]. The CCT values of Y_2O_3: Eu^{3+} (1-11 mol %) nanophosphor were calculated according to literature [47, 48] and summarized in Table.5. The CCT diagram of Y_2O_3: Eu^{3+} (1-11 mol %) nanophosphor was shown in Fig.12 (d).The effect of Eu^{3+}ions on the colour purity of phosphor was also analyzed using the relation [49]:

$$color\ \ purity = \frac{\sqrt{(x_s - x_i)^2 + (y_s - y_i)^2}}{\sqrt{(x_d - x_i)^2 + (y_d - y_i)^2}} \times 100\% \qquad \text{---------- (7)}$$

where (x_s, y_s) ; the coordinates of a sample point, (x_d, y_d) ; the coordinates of the dominant wavelength and (x_i, y_i) ; the coordinates of the illuminant point. The color purity of the synthesized samples were estimated and listed in Table.5, The above results indicate that the present phosphor may be quite useful for warm amber gap phosphor for solid state and LED's applications.

4. Conclusion

Eu^{3+} (1-11 mol %) doped Y_2O_3 nanophosphors were synthesized by ultrasound assisted sonochemical route using *A. V.* gel as a surfactant. PXRD and Rietveld refinement results confirm the increase in crystallinity with occupancy of Eu^{3+} ions in the symmetric site of the Y_2O_3 nanophosphor. Morphology of the prepared samples can be manipulated by adjusting various experimental parameters such as sonication time, concentration of *A. V.* gel, pH values and sonication power. The phosphor displays intense red emission at ~ 613 nm due to the Eu^{3+} ions corresponds to $^5D_0 \rightarrow {}^7F_2$ transition. The luminescence intensity increased with Eu^{3+} concentration up to 5 mol % and then decreases due to concentration quenching effect.

The morphology of the samples have a remarkably effect on the photoluminescence properties of the phosphor. The estimated photometric properties confirm that the material emits warm pure red color and quite useful for warm amber gap phosphor for solid state and LED's applications.

Acknowledgement

The author Dr. H Nagabhushana thanks to VGST, Karnataka (No. VGST/KFIST L-1/2016-17/GRD-489) for the sanction of this research project.

References

[1] G. Adachi, N. Imanaka, Chem. Rev. 98 (1998) 1479–1514.
[2] C. Waite, R. Mann and A. L. Diaz, J. Solid State Chem. 198 (2013) 357-363.
[3] Z. Chen, Y. W. Yan, J. M. Liu, Y. Yin, H. Wen, G. Liao, C. Wu, J.Zao, D. Liu, H. Tian, C. Zhang, S. Li, J. Alloys Compd. 478 (2009) 679–683.
[4] Quan Liu, Jialin Shen, Tian Xu, Lixi Wang, Jing Zhang, Qitu Zhang, Le Zhang, Int.42 (2016) 13855-13862.
[5] Le Zhang, Bingheng Sun, Quan Liu, Nan Ding, Hao Yang, Lixi Wang, Qitu Zhang, J. Alloy Compd. 657 (2016) 27-31.
[6] J Xu, DA Hassan, R Zeng, D Peng, Mater. Res. Bull. 71 (2015) 106-110.
[7] E.F. Schubert, J.K. Kim, Science. 308 (2005) 1274–1278.
[8] S. Neeraj, N. Kijima, A.K. Cheetham, Chem. Phys. Lett. 387 (2004) 2–6.
[9] Timothy J. Mason, Ultrason. Sonochem. 7 (2000) 145-149.
[10] Garima Ameta, Arpit Kumar Pathak, Chetna Ameta, Rakshit Ameta, Pinki B. Punjabi, J. Mol. Liq. 211 (2015) 934 - 937.
[11] J. G. Bartholomew, K. O. Lima, A. Ferrier, P. Goldner, Nano. Lett., 17 (2017) 778-787.
[12] N.D. Q. Anh, H. Y. Lee, T. T. Phuong, N. H. K. Nhan, T. H. Q. Minh, T. H. Ly, J. Chinese. Institute of Engg., (2017) http://dx.doi.org/10.1080/02533839.2017.1299592.
[13] Y. Jin, H. P. Zhou, M. S. Jiang, J. Nanosci. Nanotechnol. 16 (2016) 704 – 708.

[14] J. H. Wang, Z. P. Li, B. Liu, B. B. Liu, Chin. Phys. B, 26 (2017) 026101-6
[15] V. V. Bakovets, I. V. Yushina, O.V. Antonova, T. A. Pomelova, Optics and Sepctroscopy, 121 (2016) 862-866.
[16] Z. Li, H. Xu, B. Liu, Q. Song, Q. Zhou, H. Song, B. Liu, Phys. Status Solidi B, (2016) 1-5. DOI 10.1002/pssb.201600311.
[17] Hangxun Xu, Brad W. Zeiger, Kenneth S. Suslick, Chem. Soc. Rev. 42 (2013) 2555-2567.
[18] Ekaterina V. Skorb, Daria V. Andreevac, J. Mater. Chem. A. 1 (2013) 7547-7557.
[19] Tarek Alammar, Joanna Cybinska, Paul S. Campbell, Anja - Verena Mudring, J. Lumin. 169 (2016) 587-593.
[20] K. S. Suslick, Science. 247 (1990) 1439-1445.
[21] K. S. Suslick, J. Am. Chem. Soc. 118 (1996) 11960-11968.
[22] R. Hari Krishna, B.M. Nagabhushana, H. Nagabhushana, R.P.S. Chakradhar, R. Sivarama krishna, C. Shiva kumara, Tiju Thomas, J. Alloys Compd. 585 (2014) 129–137.
[23] G.K. Williamson, W.H. Hall, Acta Metall. 1 (1953) 22–31.
[24] R.B. Basavaraj, H. Nagabhushana, B. Daruka Prasad, S.C. Sharma, S.C. Prashantha, B.M. Nagabhushana, Optik. 126 (2015) 1745-1756.
[25] S. Som, S.K. Sharma, J. Phys. D: Appl.Phys. 45 (2012) 415102 - 415113.
[26] G.P. Darshan, H.B. Premkumar, H. Nagabhushana, S.C. Sharma, S.C. Prashantha, B. Daruka Prasad, J. Colloid Interface Sci. 464 (2016) 206 – 218.
[27] D. Kavyashree, C.J. Shilpa, H. Nagabhushana, B. Daruka Prasad, G.L. Sreelatha, S.C. Sharma, S. Ashoka, R. Anandakumari, H.B. Premkumar, ACS Sustainable Chem. Eng.3 (6) (2015) 1066–1080.
[28] M. Venkataravanappa, H. Nagabhushana, B. Daruka Prasad, G.P. Darshan, R.B. Basavaraj, G.R. Vijayakumar, Ultrason Sonochem. 34 (2017) 803–820.
[29] H.B. Premkumar, H. Nagabhushana, S.C. Sharma, S.C. Prashantha, H.P. Nagaswarupa, B.M. Nagabhushana, R.P.S. Chakradhar, J. Alloys Compd. 601 (2014) 75–84.
[30] A. Lakshmanan, R.S. Bhaskar, P.C.Thomas, R. Satheesh Kumar, V. Siva Kumar, M.T. Jose, Mats. Letts. 64 (2010) 1809–1812.
[31] L. Zhou, B. Yan, J. Phys. Chem. Solid. 69 (2008) 2877–2882.
[32] G.H. Lee, S. Kang, J. Lumin. 131 (2011) 2606–2611.
[33] G.P. Darshan, H.B. Premkumar, H. Nagabhushana, S.C. Sharma, B. Daruka Prasad, S.C. Prashantha, J. Alloys Compd. 686 (2016) 577 – 587.
[34] G. Blasse, J. Solid State Chem. 62 (1986) 207–211.
[35] D.L. Dexter, J. Chem. Phys. 21 (1953) 836–850.
[36] G. Blasse and B. C. Grabmarier, Springer-Verlag, Berlin, 1994, p. 99.
[37] B.R. Judd, Phys. Rev. 127 (1962) 750-761.
[38] G.S. Ofelt, J. Chem. Phys. 37 (1962) 511-520.
[39] N. Rakov, D.F. Amaral, R.B. Guimaraes, G.S. Maciel, J. Appl. Phys. 108(2010) 073501-073506.
[40] T.A. Singanahally, S.M. Alexander, Curr. Opin. Solid State Mater. Sci. 12 (2008) 44-50.

[41] S. Som, S. Das, S. Dutta, H. G. Visser, M. K. Pandey, P. Kumar, R. K. Dubey, S. K. Sharma, RSC Adv. 5 (2015) 70887-70898.
[42] C. A. Kodaira, H. F. Brito, O. L. Malta J. Lumin. 101 (2003) 11–21.
[43] R. Ben Dhafer, A. Ben Ahmed, H. Saidi, S. Ridene, H. Bouchriha, Optik. 127 (2016) 1198-1202.
[44] Lei Zhang, Bing Zhang, Shuai Li, Qiang Zhu, Youjin Zheng, Opt. Com. 369 (2016) 171-178.
[45] G.P. Darshan, H.B. Premkumar, H. Nagabhushana, S.C. Sharma, B. Daruka Prasad, S.C. Prashantha, Dye. Pig. 134 (2016) 227-233.
[46] Janos Schanda, M Danyi, Color Res. Appl. 2 (1977) 161-163.
[47] G.P. Darshan, H.B. Premkumar, H. Nagabhushana, S.C. Sharma, S.C. Prashantha, H.P. Nagaswarup, B. Daruka Prasad, Dye. Pig. 131(2016) 268-281.
[48] C.S. McCamy, Color Res. Appl. 17 (1992) 142-144.
[49] S. Dutta, S. Som, S. K. Sharma, RSC Adv. 5 (2015) 7380.

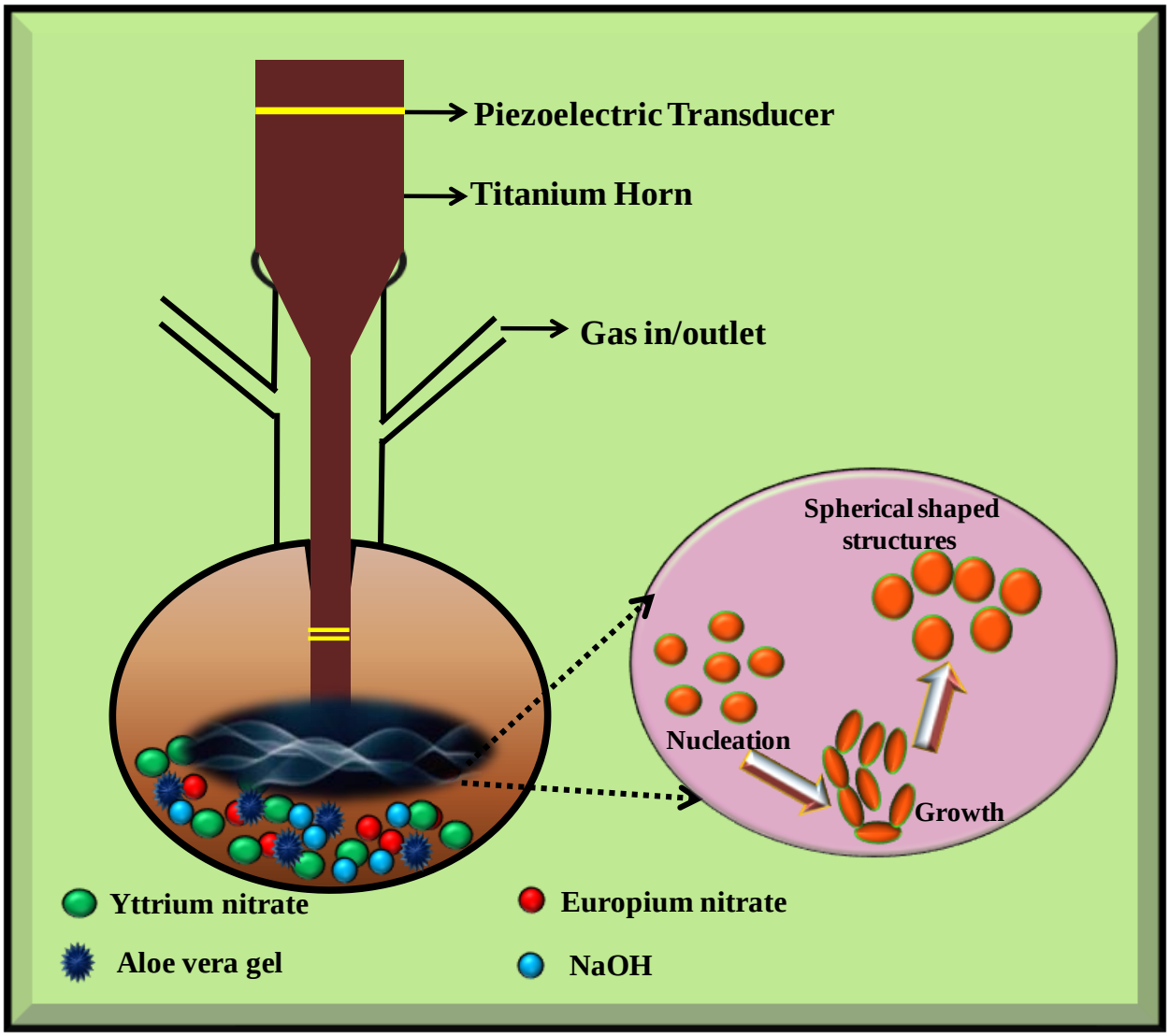

Fig.1 Schematic diagram of Eu^{3+} doped Y_2O_3 nanophosphor synthesizedby ultrasound assisted sonochemical method.

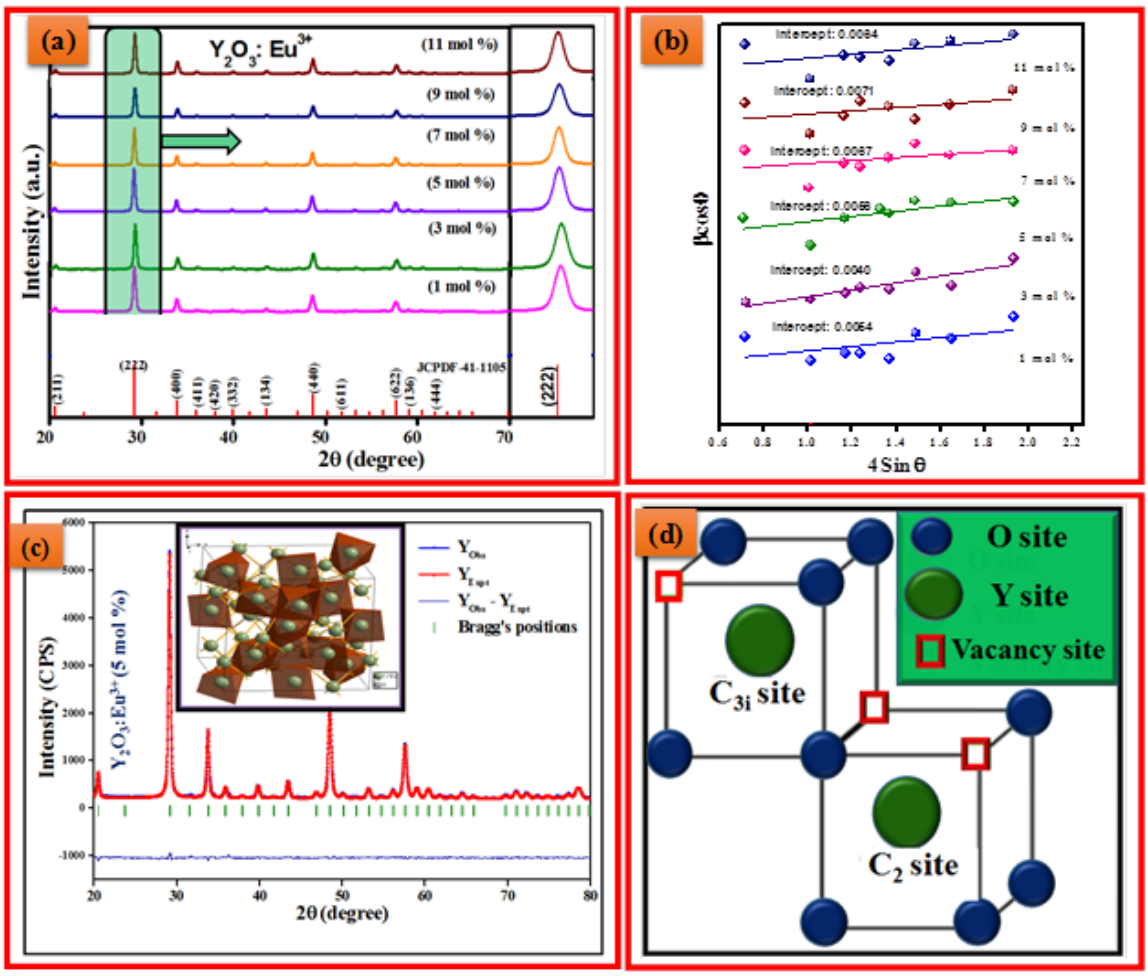

Fig.2 (a) PXRD patterns and (b) W-H plots, for the $Y_2O_3:Eu^{3+}$ (1-11 mol %) nanophosphor, (c) Rietveld refinement pattern (Inset: the schematic representation of the cubic unit cell of Y_2O_3)for $Y_2O_3:Eu^{3+}$ (5 mol %) nanophosphor synthesized with 20 kHz sonication power, 6 h sonication time, 30 % W/V surfactant and pH of 9. (d) cationic symmetry site

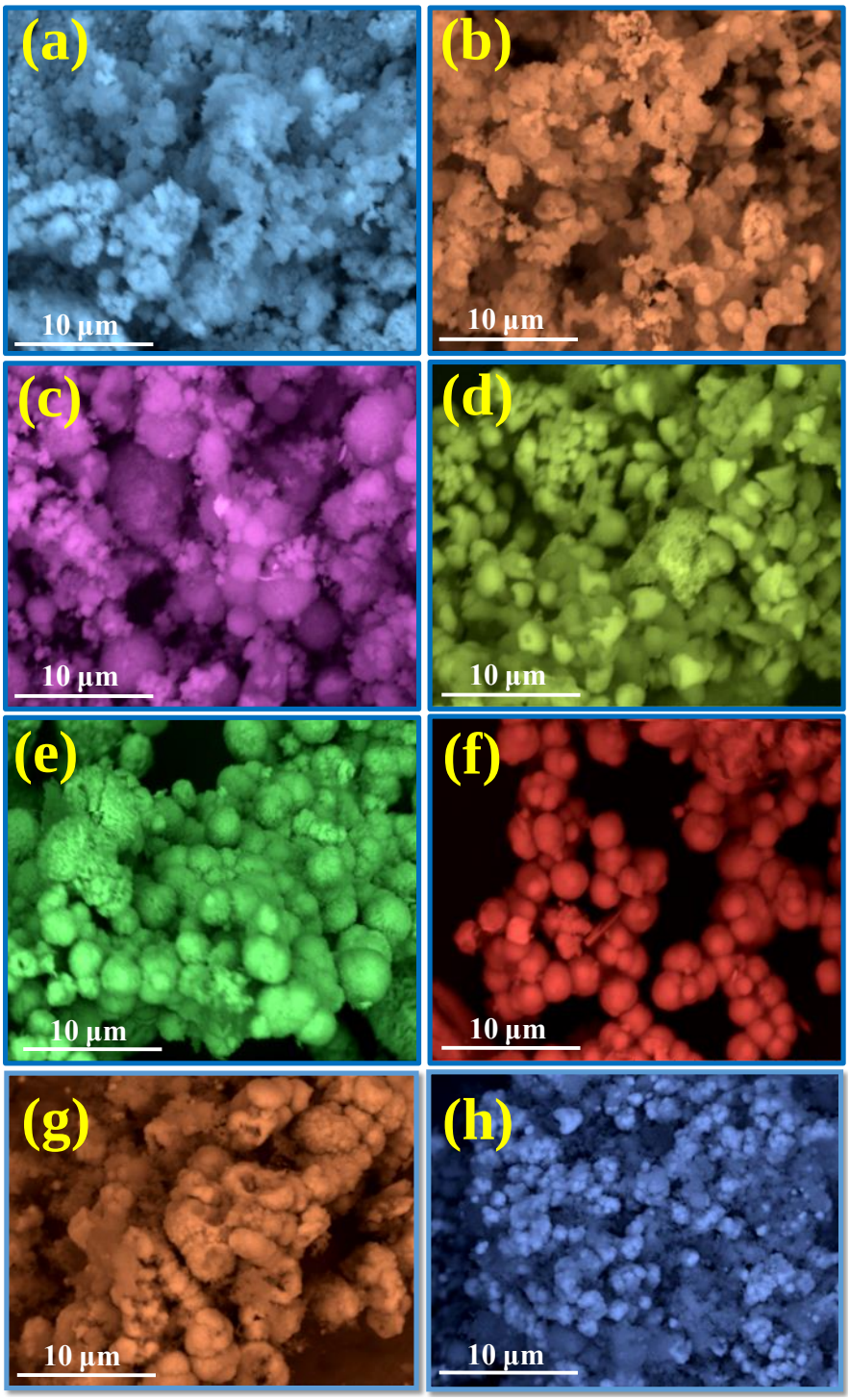

Fig.3. SEM images of Y_2O_3: Eu^{3+} (5 mol %) nanophosphor synthesized with different sonication time (1 h, 2 h, 3 h, 4 h, 5 h, 6 h, 7 h and 8 h) with 30 % W/V *A.V.* gel, sonication power of 20 kHz and pH of 9**.**

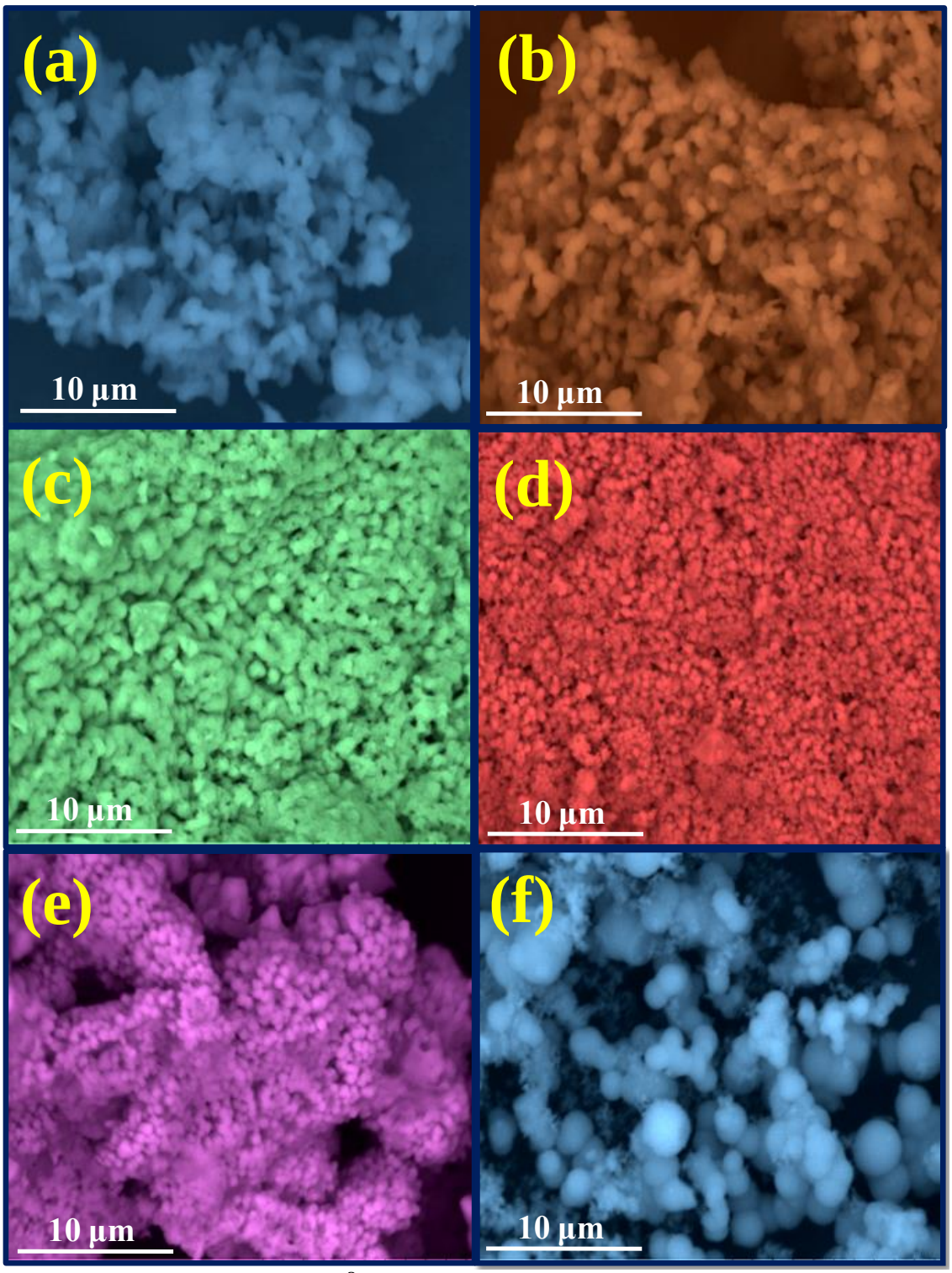

Fig.4. SEM images of Y_2O_3: Eu^{3+} (5 mol %) nanophosphor synthesized with different concentration of *A.V.* gel (a) 5 % W/V, (b)10 % W/V, (c)15 % W/V, (d) 20 % W/V, (e) 25 % W/V and (f) 30 % W/V while sonication time, sonication power and pH were fixed at 6 h, 20 kHz and 9 respectively.

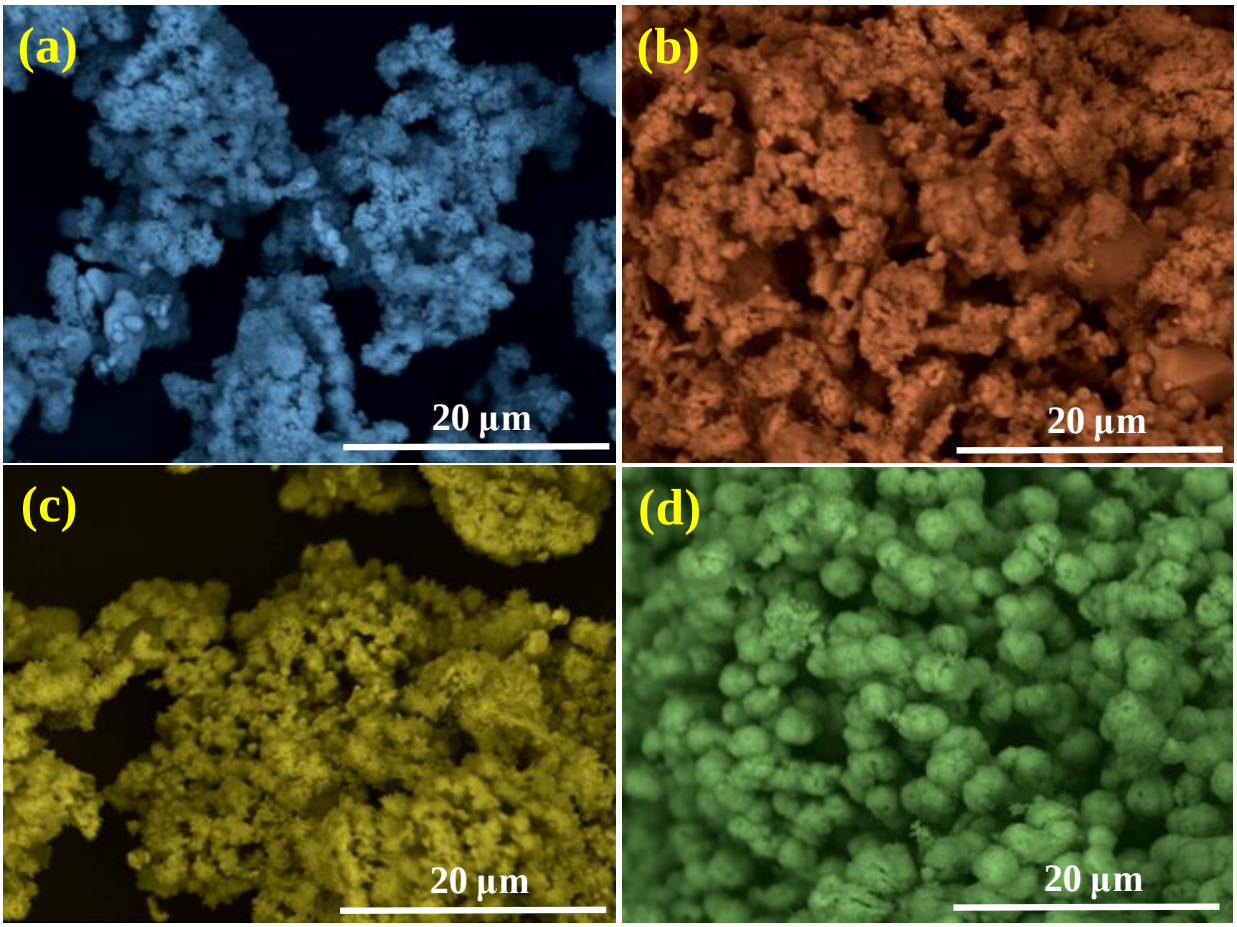

Fig.5. SEM images of $Y_2O_3:Eu^{3+}$ (5 mol %) nanophosphor synthesized with various pH values of (a) 1, (b) 5, (c) 7 and (d) 9 while sonication time and concentration of *A.V.* gel were fixed at 6 h and 30 ml respectively.

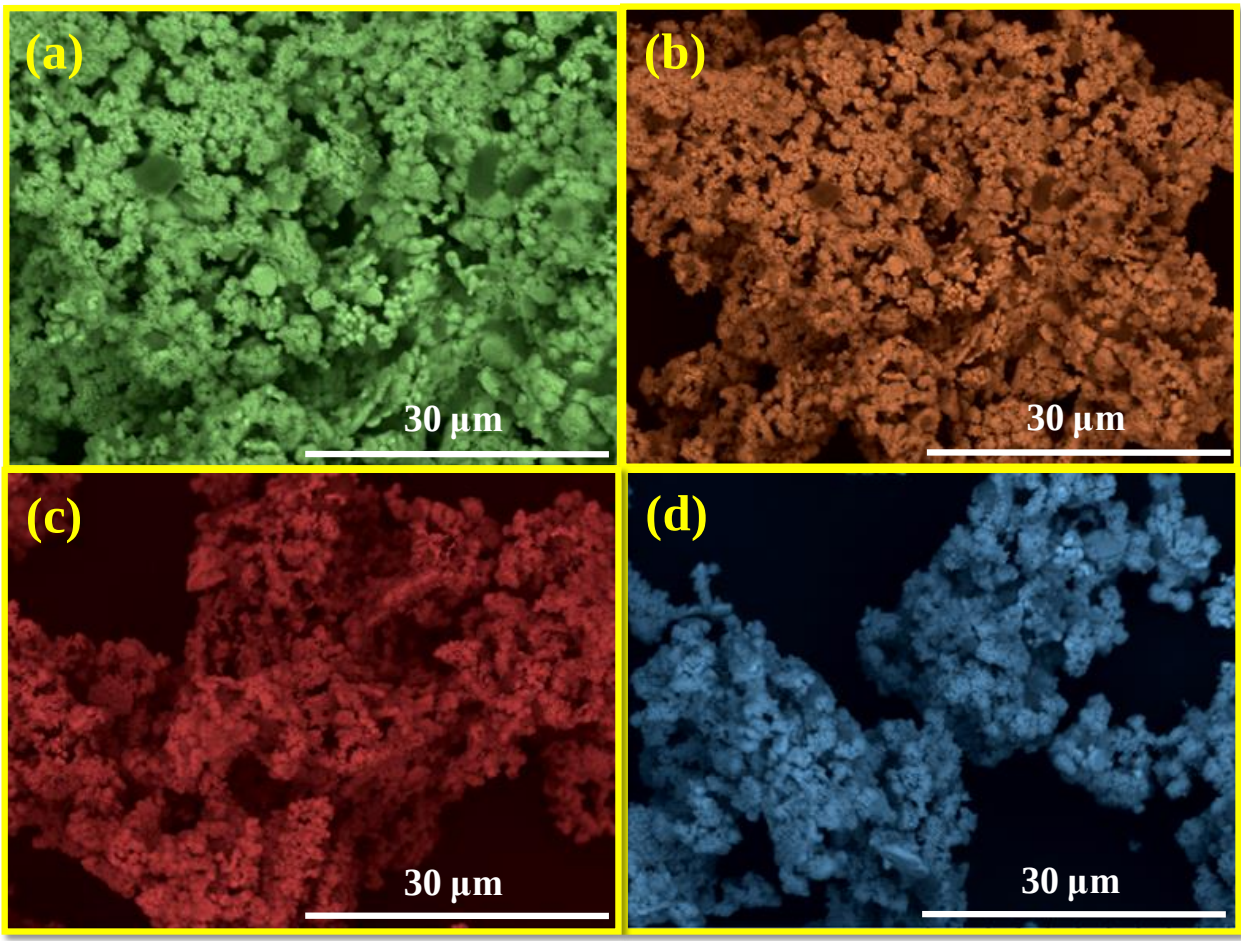

Fig.6. SEM images of $Y_2O_3:Eu^{3+}$ (5 mol %) nanophosphor synthesized with different sonication power (a) 20, (b) 24, (c) 26 and (d) 28 kHz with 6 h sonication time, 30 ml *A.V.* gel concentration and pH = 9.

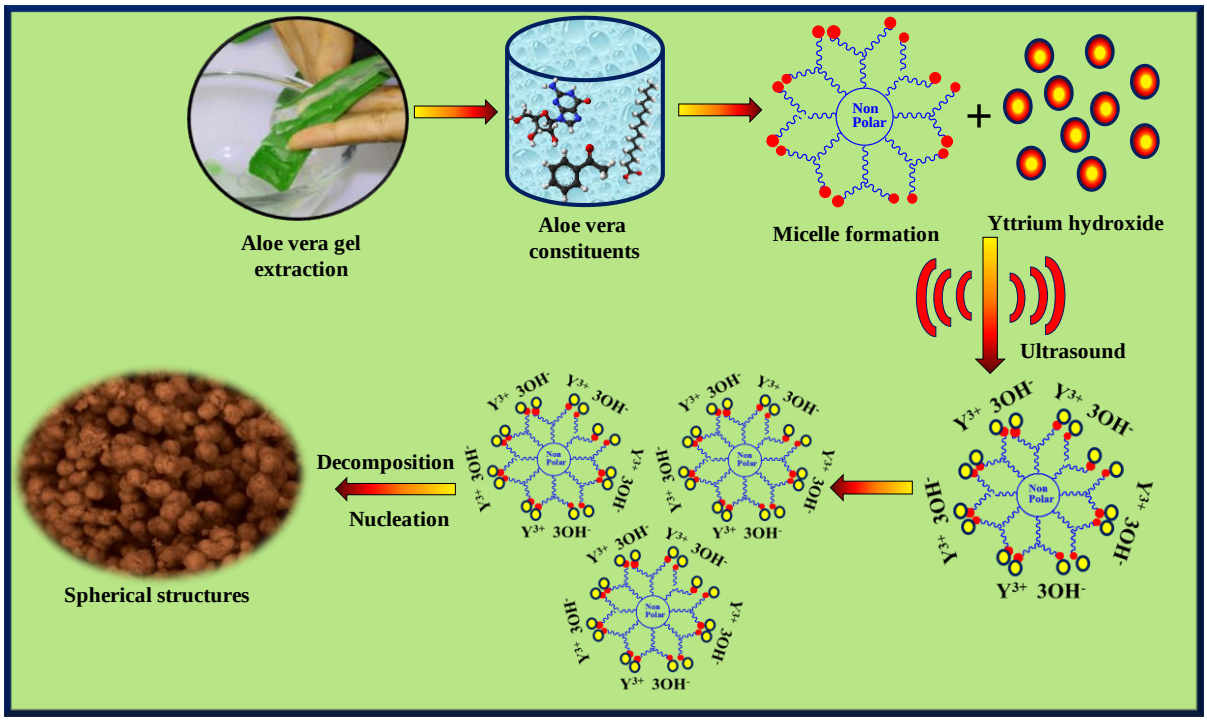

Fig.7.Schematic representation of Y_2O_3: Eu^{3+}structures in the presence of surfactant *A.V.* gel.

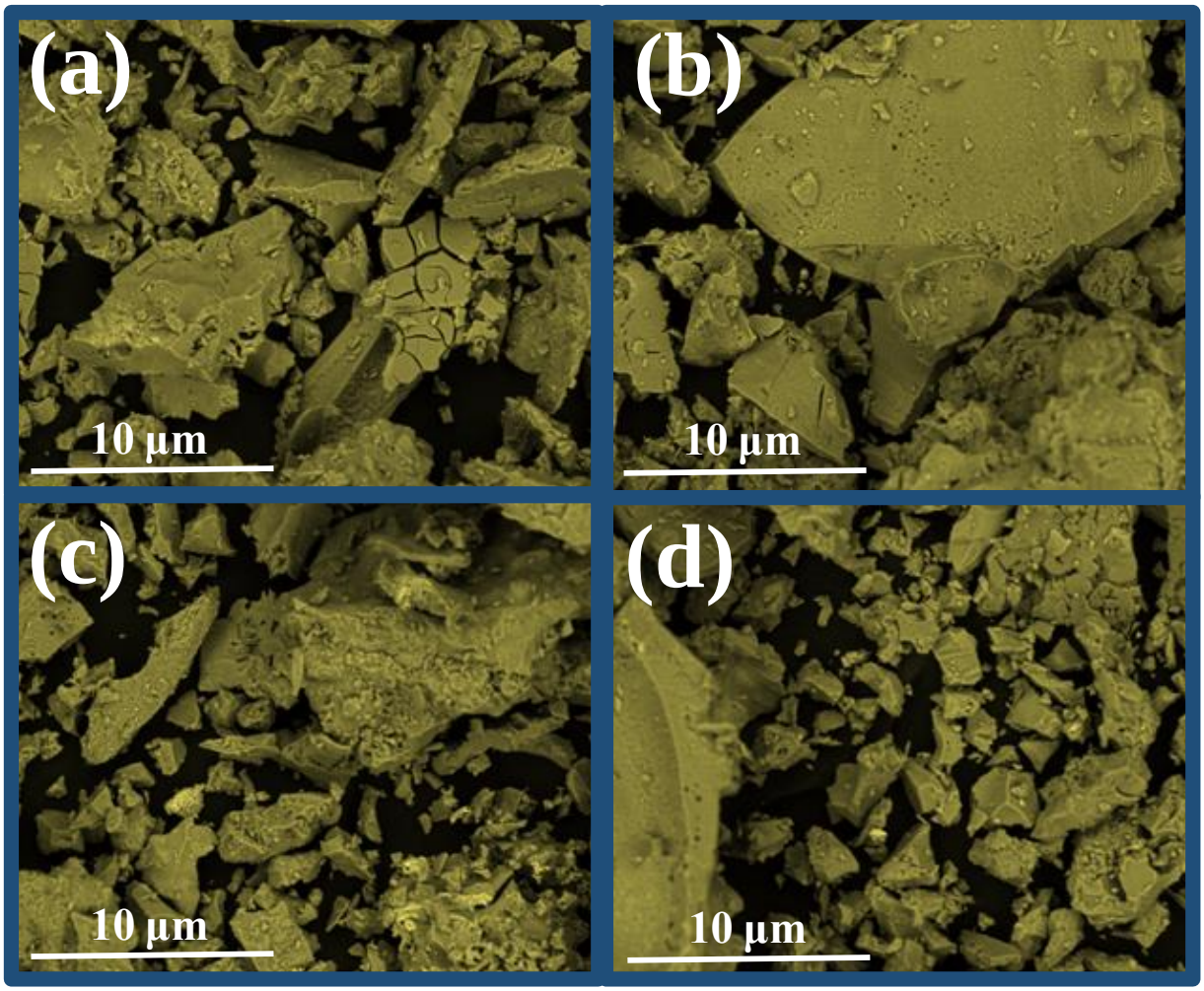

Fig.8.SEM micrographs of $Y_2O_3:Eu^{3+}$ (5 mol %) nanophosphor synthesized with sonication time of (a) 2 h, (b) 3 h ,(c) 5 h and (d) 6 h with pH = 9, sonication power of 20kHz and without any surfactant.

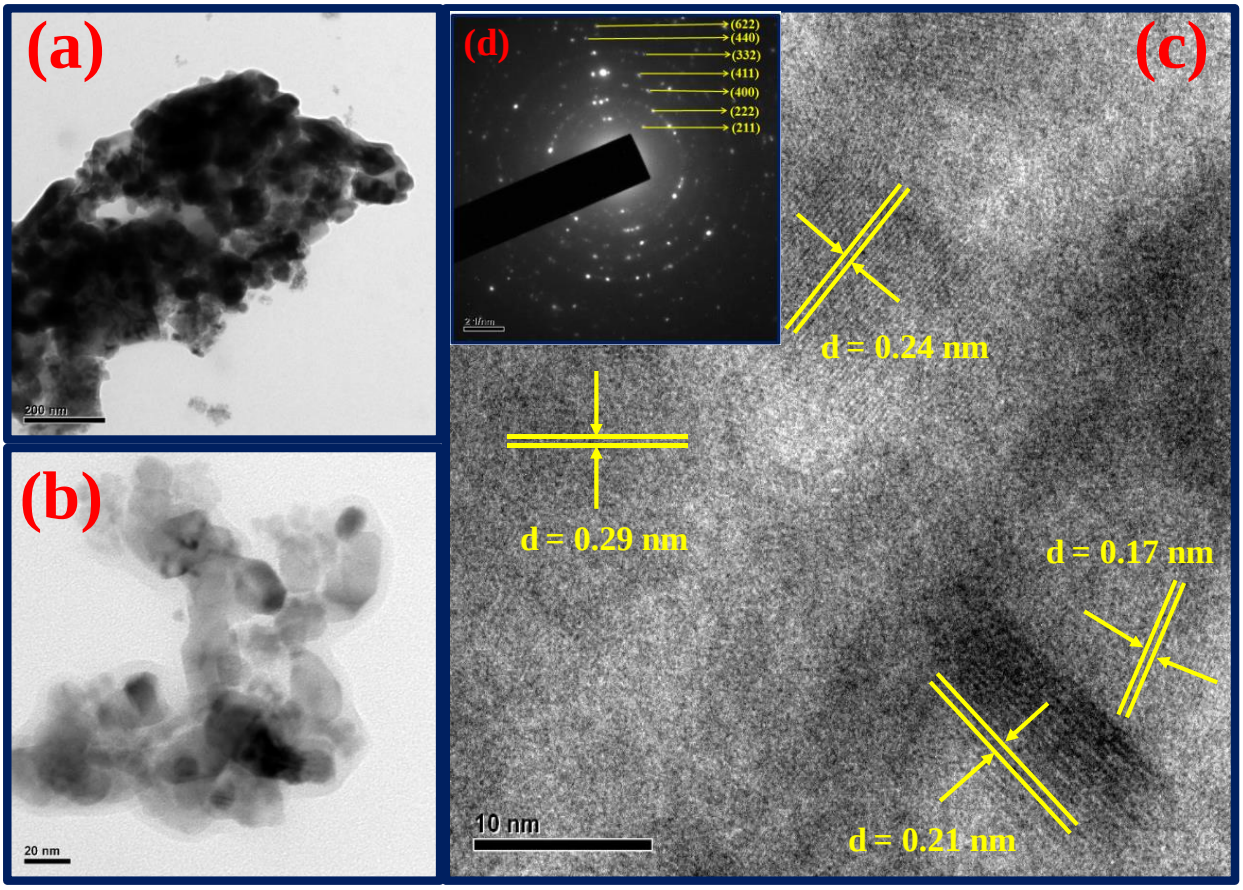

Fig.9 (a, b) TEM, and (c) HRTEM (inset (d) SAED) images of $Y_2O_3:Eu^{3+}$ (5 mol %) nanophosphor for pH = 9, sonication power of 20kHz, sonication time of 6 h and A.V. gel of 30% W/V.

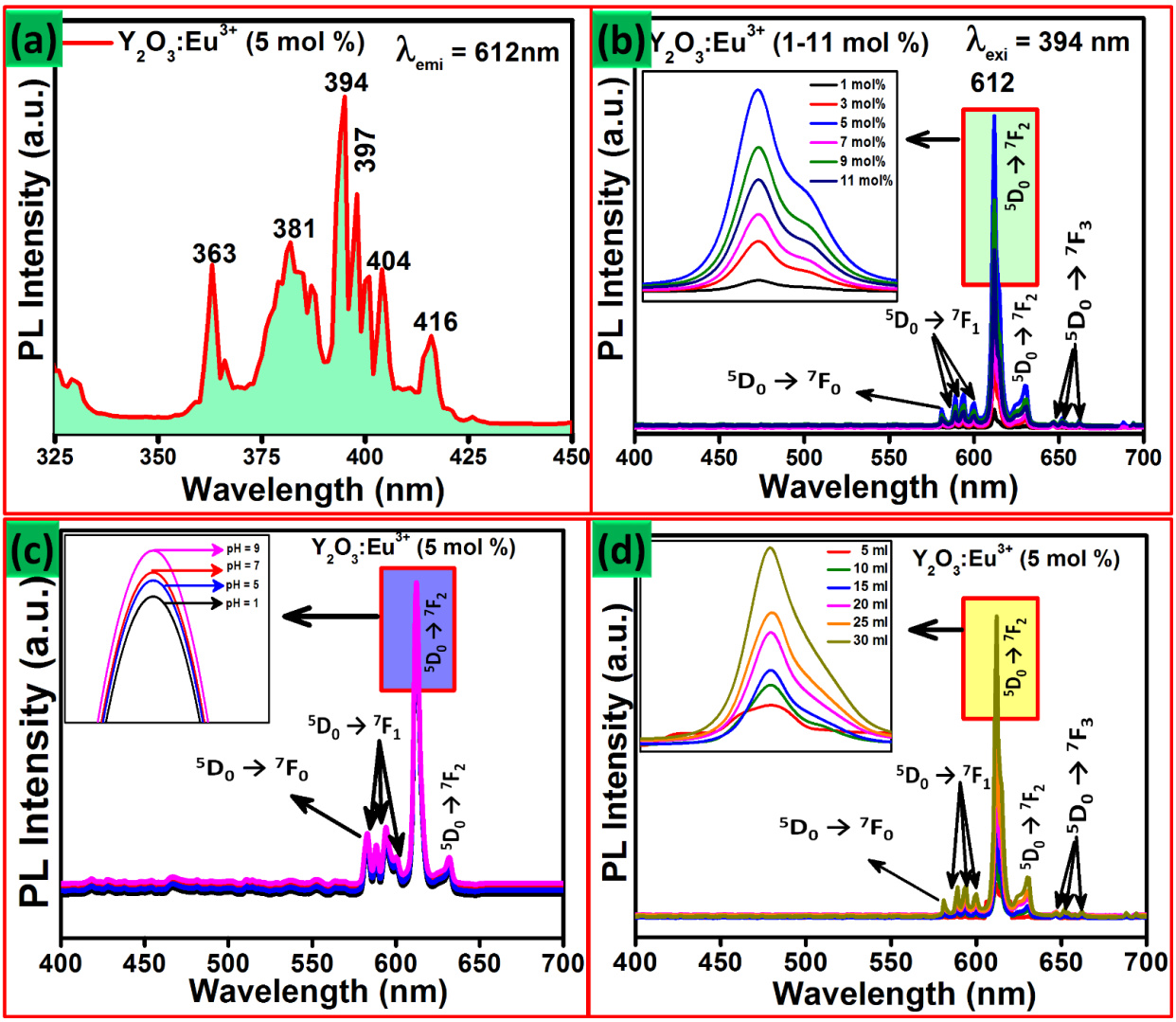

Fig.10 (a) PL excitation spectrum of $Y_2O_3:Eu^{3+}$ (5 mol %) nanophosphor under emission wavelength 612 nm **(b)** Emission spectra of $Y_2O_3:Eu^{3+}$(1-11 mol %) nanophosphor excited at λ_{exi}= 394 nm, **(c)** emission spectra of $Y_2O_3:Eu^{3+}$ (5 mol %) nanophosphor synthesized at different pH value with sonication power, time and *A.V.* gel concentration of 20 kHz, 6 h and 30 % W/V respectively, and **(d)** emission spectra of $Y_2O_3:Eu^{3+}$ (5 mol %) nanophosphor synthesized at different *A.V.* gel concentration with sonication power, time and pH of 20 kHz, 6 h and 9 respectively.

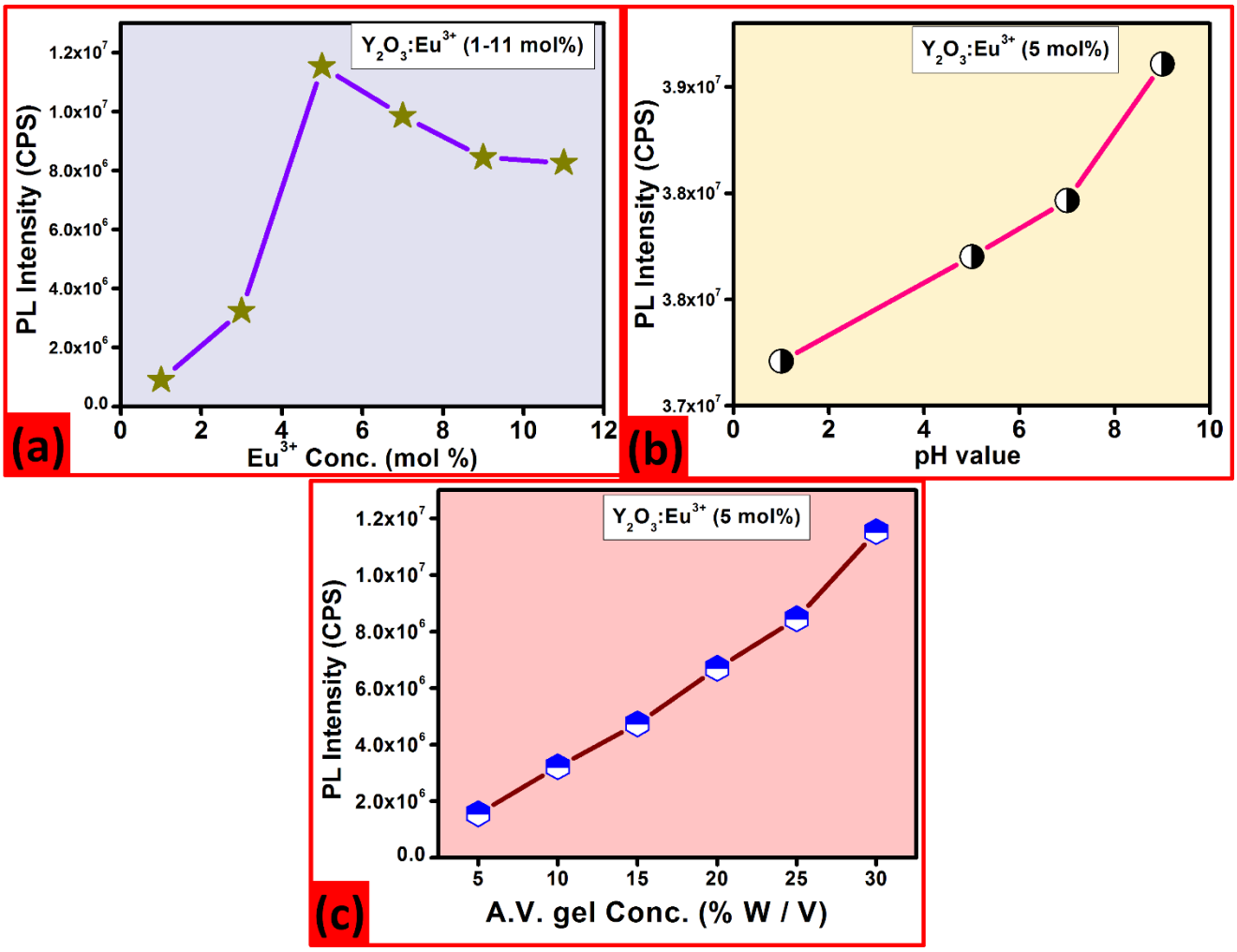

Fig.11. Variation of PL intensity at 612 nm with respect to **(a)** Eu^{3+} concentration for the samples prepared with pH of 9 and *A.V.* gel concentration of 30 % W/V **(b)** various pH values and *A.V.* gel concentration of 30 % W/V **(c)** *A.V.* gel concentration and pH value of 9 (sonication power of 20 kHz and sonication time of 6 h are as common parameters)

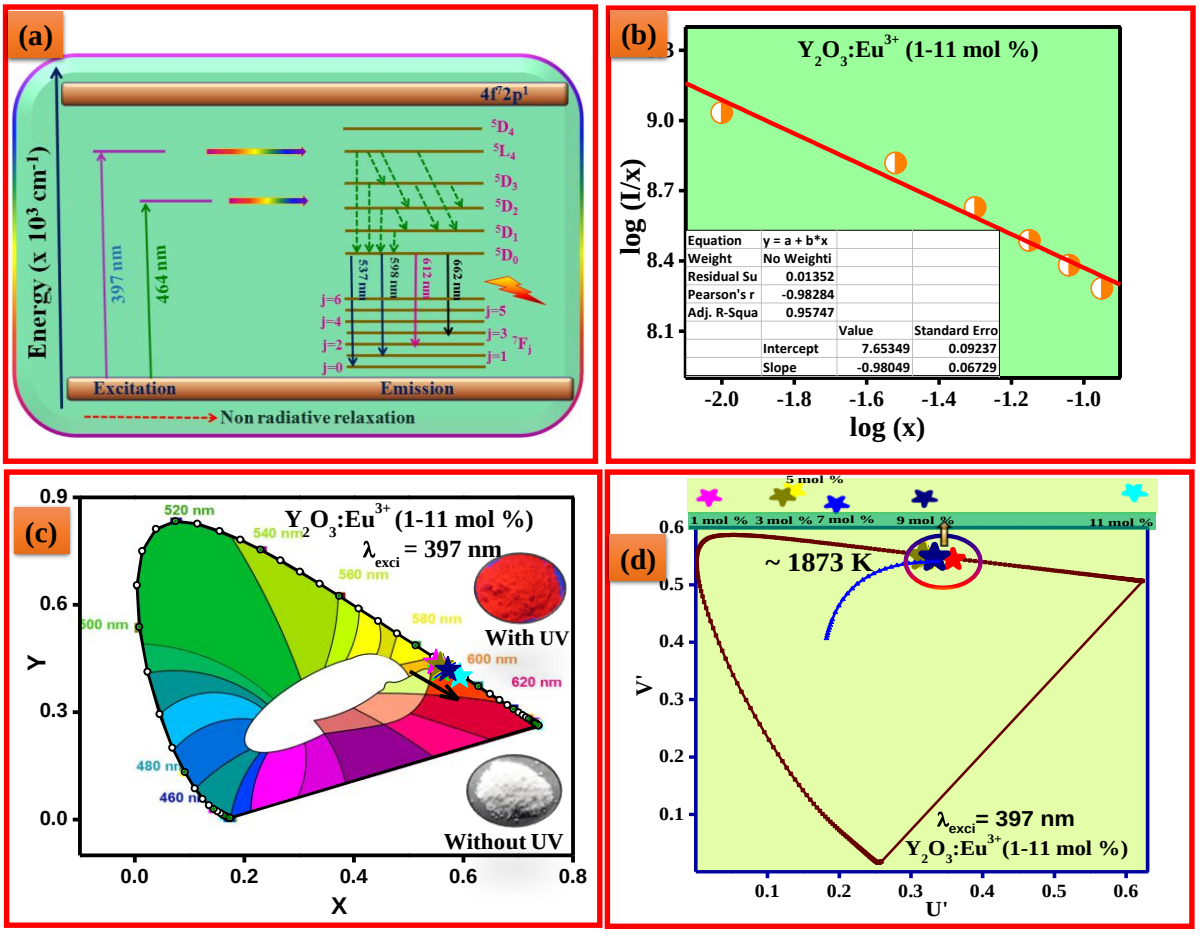

Fig.12 (a) Energy level diagram (b) Logarithmic plot of I/X as a function of the dopant concentration (X) (c) CIE and (d) CCT diagram of $Y_2O_3:Eu^{3+}$ (1– 11 mol %) nanophosphor prepared with pH of 9, *A.V.* gel concentration of 30 % W/V, sonication power of 20kHz and sonication time of 6 h.

Table.1.Estimated average crystallite size (Scherrer's and W-H plots), strain, dislocation density and surface factor of Y_2O_3:Eu^{3+}(1-11 mol %) nanophosphor.

Eu^{3+} conc. (mol%)	**Particle size (nm)**		**Micro strain ε (10^{-3} $lin^{-2}m^{-4}$)**	**Lattice strain ϵ (x10^{-3})**
	Scherrer's relation (d)	**W-H plots (D)**		
Pure	7	8	07.5	07.9
1	4	8	13.3	11.5
3	4	7	13.6	12.2
5	4	7	15.1	14.9
7	4	6	15.9	15.2
9	4	6	15.9	15.6
11	4	6	16.1	15.8

Table.2 Rietveld refinement of the Y_2O_3compound prepared with different concentration of trivalent (Eu^{3+}) dopant.

Compounds	**Y_2O_3:** Eu^{3+} (1 mol %)	**Y_2O_3:** Eu^{3+} (3 mol %)	**Y_2O_3:** Eu^{3+} (5 mol %)	**Y_2O_3:** Eu^{3+} (7 mol %)	**Y_2O_3:** Eu^{3+} (9 mol %)	**Y_2O_3:** Eu^{3+} (11 mol %)
Crystal system	Cubic	Cubic	Cubic	Cubic	Cubic	Cubic
Space group	I a -3 (206)	I a -3 (206)	I a -3 (206)	I a -3 (206)	I a -3 (206)	I a -3 (206)
a = b = c	10.6221	10.6218	10.6186	10.6172	10.6196	10.6217
Unit cell volume ($Å^3$)	1198.48	1198.38	1197.30	1196.82	1197.64	1198.35
Y1 (Wyckoff – 24d)						
x	-0.03009	-0.0299	-0.0299	-0.0299	-0.0299	-0.0299
y	*0*	*0*	*0*	*0*	*0*	0
z	*0.25*	*0.25*	*0.25*	*0.25*	*0.25*	0.25
Occupancy	0.50038	0.46242	0.4483	0.45342	0.43951	0.43948
Eu1 (Wyckoff – 24d)						
x	-0.03009	-0.0299	-0.0299	-0.0299	-0.0299	-0.0299
y	*0*	*0*	*0*	*0*	*0*	0
z	*0.25*	*0.25*	*0.25*	*0.25*	*0.25*	0.25
Occupancy	0.1112	0.1112	0.1112	0.1112	0.1112	0.1112
Y2 (Wyckoff - 8b)						
x	-0.03009	-0.02990	-0.02990	-0.02990	-0.0299	-0.0299
y	*0*	*0*	*0*	*0*	*0*	0
z	*0.25*	*0.25*	*0.25*	*0.25*	*0.25*	0.25
Occupancy	0.1112	0.1112	0.1112	0.1112	0.1112	0.1112
Eu2 (Wyckoff - 8b)						
x	0.25	0.25	0.25	0.25	0.25	0.25
y	0.25	0.25	0.25	0.25	0.25	0.25
z	*0.25*	*0.25*	*0.25*	*0.25*	*0.25*	0.25
Occupancy	0.1627	0.1445	0.1403	0.1520	*0.1456*	0.1456
O1 (Wyckoff – 48e)						
x	0.25	0.25	0.25	0.25	0.25	0.25
y	0.25	0.25	0.25	0.25	0.25	0.25
z	*0.25*	*0.25*	*0.25*	*0.25*	*0.25*	0.25
Occupancy	*0.034*	*0.034*	*0.035*	*0.033*	*0.033*	0.034
R_P	2.71	2.66	2.17	2.49	2.45	2.77
R_{WP}	3.61	3.56	3.97	3.28	3.47	4.67
R_{Exp}	4.71	4.08	4.04	4.64	4.77	5.71
GoF	0.77	0.87	0.98	0.71	0.73	0.82
R_{Bragg}	2.57	1.71	2.17	1.78	2.27	1.63
R_F	2.41	2.07	2.22	2.18	2.47	2.57
X-ray density (g/cc^3)	5.713	5.556	5.548	5.579	5.715	5.707

Table.3.J-O intensity parameters (Ω_2, Ω_4), radiative transition probability (A_T), estimated radiative life time (τ_{rad}), branching ratio (β) and asymmetric ratio (A_{21}) of Y_2O_3:Eu^{3+}(1-11 mol %) nanophosphor.

J–O intensity

Eu^{3+} conc. (mol %)	parameters ($\times 10^{-20}$ cm^2)		A_T (s^{-1})	τ_{rad} (ms)	β (%)	Asymmetry ratio (A_{21})
	Ω_2	Ω_4				
1	1.35	4.11	246	4.07	21	5.39
3	1.53	6.60	284	3.52	18	4.79
5	1.11	5.18	209	4.79	16	3.94
7	6.31	5.80	200	7.77	09	2.23
9	4.46	6.59	198	1.00	08	1.58
11	3.39	7.01	180	1.20	06	1.20

Table.4.Effective bandwidth ($\Delta\lambda_{eff}$), stimulated emission cross-section (σ_e), gain bandwidth (σ_e x $\Delta\lambda_{eff}$) and optical gain (σ_e x τ_{rad}) of Y_2O_3:Eu^{3+}(1-11 mol%) nanophosphor.

Eu^{3+} conc. (mol%)	**Transition**	**Δ_{eff} (nm)**	**σ_e (10^{-22} cm^2)**	**$\sigma_e x \Delta_{eff}$ (10^{-28} cm^3)**	**$\sigma_e x \tau_{rad}$ (10^{-25} cm^2 s^{-1})**
1	$^5D_0 \rightarrow {}^7F_0$	8	1.71	1.37	6.95
	$^5D_0 \rightarrow {}^7F_1$	5	3.16	1.58	1.11
	$^5D_0 \rightarrow {}^7F_2$	6	7.71	4.63	9.26
	$^5D_0 \rightarrow {}^7F_3$	9	1.29	1.16	6.18
	$^5D_0 \rightarrow {}^7F_4$	13	5.50	7.15	4.28
3	$^5D_0 \rightarrow {}^7F_0$	6	2.28	1.37	9.26
	$^5D_0 \rightarrow {}^7F_1$	6	2.63	1.58	9.26
	$^5D_0 \rightarrow {}^7F_2$	6	9.27	5.56	9.26
	$^5D_0 \rightarrow {}^7F_3$	8	1.45	1.16	6.95
	$^5D_0 \rightarrow {}^7F_4$	7	1.02	7.15	7.94
5	$^5D_0 \rightarrow {}^7F_0$	8	1.71	1.37	6.95
	$^5D_0 \rightarrow {}^7F_1$	7	2.26	1.58	7.94
	$^5D_0 \rightarrow {}^7F_2$	9	1.29	1.16	6.18
	$^5D_0 \rightarrow {}^7F_3$	8	1.45	1.16	6.95
	$^5D_0 \rightarrow {}^7F_4$	13	5.50	7.15	4.28
7	$^5D_0 \rightarrow {}^7F_0$	7	1.95	1.37	7.94
	$^5D_0 \rightarrow {}^7F_1$	7	2.26	1.58	7.94
	$^5D_0 \rightarrow {}^7F_2$	9	1.52	1.37	6.18
	$^5D_0 \rightarrow {}^7F_3$	9	1.29	1.16	6.18
	$^5D_0 \rightarrow {}^7F_4$	11	6.50	7.15	5.05
9	$^5D_0 \rightarrow {}^7F_0$	6	2.28	1.37	9.26
	$^5D_0 \rightarrow {}^7F_1$	7	2.26	1.58	7.94
	$^5D_0 \rightarrow {}^7F_2$	12	1.32	1.58	4.63
	$^5D_0 \rightarrow {}^7F_3$	9	1.29	1.16	6.18
	$^5D_0 \rightarrow {}^7F_4$	11	6.50	7.15	5.05
11	$^5D_0 \rightarrow {}^7F_0$	6	2.28	1.37	9.26
	$^5D_0 \rightarrow {}^7F_1$	6	2.63	1.58	9.26
	$^5D_0 \rightarrow {}^7F_2$	12	5.96	7.15	4.63
	$^5D_0 \rightarrow {}^7F_3$	9	1.29	1.16	6.18
	$^5D_0 \rightarrow {}^7F_4$	10	7.15	7.15	5.56

Table.5. Photometric characteristics of Y_2O_3:Eu^{3+} (1-11 mol %) nanophosphor.

Eu^{3+} (mol %)	**CIE**		**CCT**		**CCT (K)**	**CRI (%)**
	X	**Y**	**$U^{/}$**	**$V^{/}$**		
1	0.562	0.426	0.3216	0.5486	1894	83.12
3	0.593	0.412	0.3586	0.5443	1749	84.10
5	0.550	0.438	0.3074	0.5508	2020	88.33
7	0.561	0.436	0.3181	0.5497	1922	84.12
9	0.558	0.431	0.3163	0.5497	1937	83.17
11	0.572	0.418	0.3329	0.5474	1820	81.22